Available online at www.sciencedirect.com
ScienceDirect
Journal of Magnetic Resonance 182 (2006) 66–74
JMR Journal of Magnetic Resonance
www.elsevier.com/locate/jmr

Sample-specific diamagnetic and paramagnetic passive shimming

Kevin M. Koch *, Peter B. Brown, Douglas L. Rothman, Robin A. de Graaf

Magnetic Resonance Research Center, Yale University, New Haven, CT, USA

Received 10 February 2006; revised 7 June 2006
Available online 30 June 2006

Abstract

When homogenizing the static magnetic field over extended *in vivo* volumes, significant residual inhomogeneity can remain after spherical harmonic shim optimization. This is due to the low spatial orders of shims available on *in vivo* MR systems and the presence of higher-order inhomogeneity in the vicinity of anatomic air cavities. Mediation of this problem through the development of higher-order spherical harmonic shims is severely impeded by bore space limitations. Sample-specific passive shims are not limited to low-order spatial compensation and offer an alternative means to increased homogenization. Here, we present a novel construction protocol for sample-specific passive shims comprised of both diamagnetic (bismuth) and paramagnetic (zirconium) materials. A prototype shim is constructed and shown to significantly homogenize the mouse brain at 9.4 T. Further homogenization capabilities are simulated through alteration of the shim construction.

Keywords: B_0 homogeneity; Shimming; Passive shimming

1. Introduction

Spatial variations of magnetic susceptibility (χ_M) within a sample generate static magnetic induction fields which compromise B_0 homogeneity. Direct compensation for B_0 inhomogeneity can be accomplished in two manners, known as active or passive shimming. Active shimming utilizes continuously adjustable electromagnets, typically in the form of room-temperature spherical harmonic gradient coils. This has been, and remains the primary method of inhomogeneity compensation. Improvements in the construction of spherical harmonic shim coils have been extensively investigated and high-order coils are readily utilized over reduced volumes in vertical bore systems. However, higher-order shim coils are difficult to construct with significant strength over larger *in vivo* sample volumes. Within both humans and animals, this results in a lack of compensation for high-order inhomogeneity near anatomic air cavities such as the nasal sinuses and auditory tracts. Over extended volumes, the efficacy of low-order shims can be bolstered through dynamic shim updating (DSU) [1–4]. However, since it is based on spherical harmonic shim technology, DSU is ultimately limited to low-order compensation. Actively shimmed reduction of residual global inhomogeneity has also been demonstrated using localized non-spherical harmonic coils [5].

Passive shimming describes any attempt to homogenize the static magnetic field through optimal placement of specific magnetic materials. For example, the subject-independent field is typically optimized through placement of highly magnetic elements within the magnet assembly [6]. Other examples of passive shimming include diamagnetic graphite mouth-insert shims [7] and arrays of ferromagnetic materials [8]. Both approaches have demonstrated homogeneity improvement in localized regions of the human brain, but are limited in capability due to placement restrictions and the use of only a single shim material.

To further reduce sample-specific inhomogeneity over extended volumes, we have investigated an alternative passive shimming system. In this approach, two materials of opposing magnetic susceptibility are distributed to compensate targeted inhomogeneity. Materials are used which have large enough magnetic susceptibilities to generate

* Corresponding author. Fax +1 203 785 6643.
E-mail address: kevin.koch@yale.edu (K.M. Koch).

1090-7807/$ - see front matter © 2006 Elsevier Inc. All rights reserved.
doi:10.1016/j.jmr.2006.06.013

significant induction fields, yet small enough to not experience significant torques at high magnetic fields. Although a wide variety of materials satisfy these two criteria, the current implementation used bismuth ($\chi_M \approx -164$ ppm) and zirconium ($\chi_M \approx +92$ ppm) [9]. These two metals were chosen because of their relative ease to work with and availability at reasonable cost. The two-material approach provides requisite field-crafting freedom needed to compensate higher-order spatial variations. In comparison to previous passive shim approaches [6–8], the system also provides significantly more freedom in the positioning of shim materials.

Given a user-defined grid for placement of shim materials, a calculation procedure to determine optimal two-material stacks of shim elements at each position in the grid is presented. The accuracy of this calculation hinges on three approximations in the nature of the magnetic fields induced by the shim materials. Empirical measurements are presented which demonstrate the validity of these approximations in the current and proposed implementations of the shim system. Utilizing these approximations, the composition calculation is reduced to a linear problem rapidly soluble with readily available optimization algorithms. Given the aforementioned torque-free condition, this allows for real-time, active-adjustment of the shim composition.

As a validation of the principles used in the shim construction, a prototype shim was manufactured to homogenize the brain of BL C57 mice at 9.4 T. Due to its high surface to volume ratio, the mouse brain possesses some of the most severe magnetic field inhomogeneity found *in vivo*. Despite this limitation, the demand for mouse investigations in NMR has been rapidly increasing, particularly in the phenotyping of transgenic mice. The prototype construction assembly is based on readily available centrifuge tubes which are commonly utilized as mouse beds. [12] Graphical and quantitative comparisons with existing room-temperature shim technology demonstrate that the constructed shim out-performs existing shim systems.

Significant improvements in the accuracy and capability of the shim construction are proposed. Computations are presented using these propositions which demonstrate the dramatic homogenizing capability of the shim system. The improved capability of the two-material optimization over a one-material approach is also clarified within this computational framework.

2. Theory

Bismuth (Bi) and zirconium (Zr) metals are ideal passive shim materials because they have intermediate magnetic susceptibilities which induce significant B_0 perturbations, but do not experience significant torques at high magnetic fields. CRC tables [11] give molar magnetic susceptibilities for elemental Bi and Zr of -280 and $+120 \times 10^{-6}$ cm^3/mol, respectively. Shenck [9] reports absolute susceptibility values for the two metals as -164 and $+92$ ppm, respectively. The exact absolute susceptibilities of the source metals could vary with manufacture process and purity. However, the precise absolute susceptibility values of materials used within the following shim construction are inconsequential, given the empirical nature of the construction procedure.

The following approximations in the nature of magnetic fields induced by magnetic materials such as Bi and Zr are crucial in the calculation of material compositions of the shim grid.

(1) In regions not directly adjacent to the shim materials, the induction fields from shim elements (or stacks of elements) at separate shim grid positions add in linear superposition.
(2) The amplitude and shape of an induction field from a shim element is dominated by its own susceptibility and is trivially perturbed by other nearby materials with much smaller magnetic susceptibilities. This approximation is encountered *in vivo*, where air ($\chi_M \approx 0.3$ ppm) and biological tissue ($\chi_M \approx -9$ ppm) are the only other materials present.
(3) The geometric distribution of an element's induction field does not change when elements are stacked together in a limited fashion.

The physical basis of these approximations is similar to that utilized in a recently reported non-iterative magnetostatic field perturbation calculation [16,17], which is essentially a first-order, or dipole-approximation to the general magnetostatic field solution. However, to clearly establish the validity of this approach in our passive shim development, empirical measurements validating these statements are presented in the next section.

Utilizing approximations 1 and 2, an empirically measured induction field, or 'response', (the terms 'response' and induction field will henceforth be used interchangeably in this work) from a chosen stack configuration (known as the 'unit' stack, which generates a 'unit' response for each stack position) is used to determine ratios of that (unit) response for each position within a shim grid. These ratios are calculated to optimally compensate a specified target field. Approximation 3 then allows for calibrations of material stacks which provide a physical manifestation of the calculated shim configuration.

2.1. Shim construction protocol

We begin by defining $\mathcal{R}(\mathbf{r})$ as the response from a unit element ($\eta_i = 1$) at each element position, i, and each spatial position $\mathbf{r}_j$ within a target ROI. $\mathcal{R}_i(\mathbf{r}_j)$ is then an array of dimensions $N \times M$, where M is the total number of spatial points in the ROI and N is the number of stack positions on the shim former. By letting η_i scale these unit responses and applying approximation 1, the total induction field within the target region is then given by the superposition of the magnetic field induced by each position on the shim grid,

$$B_z^{\text{in}}(\mathbf{r}_j) = \sum_{i=1}^{N} \eta_i \mathcal{R}_i(\mathbf{r}_j). \quad (1)$$

Given a desired target field to compensate, $T(\mathbf{r}_j)$, we can then express the shim calculation as

$$\text{Find } \eta_i^* \text{ that minimizes } \sum_{j=1}^{M} \left[T(\mathbf{r}_j) + \sum_{i=1}^{N} \eta_i^* \mathcal{R}_i(\mathbf{r}_j) \right]^2, \quad (2)$$

where the solutions η_i^* now represent optimal response coefficients which eliminate the target field for the given shim geometry. This can be further simplified to the linear problem

$$\mathbf{T} = -\mathcal{R}\eta^*. \quad (3)$$

Physically, the components of η^* are optimal scalings of the unit element response at each grid position. Through approximation 3, calibrations allow for this scaling by stacking the two shim materials. Computational optimization constraints must be placed (1) to keep stack heights below the threshold where stacked responses begin to differ geometrically from unit responses, and (2) to keep the stack heights within the physical dimensions of the RF coil. Finally, approximation 2 assures that calibrated responses, established on a water phantom *in vitro*, will be equally valid for the generation of a compensating field on the mouse brain *in vivo*. A specific experimental protocol is now outlined to utilize this shim composition calculation.

3. Methods

All experiments were performed at the Yale Magnetic Resonance Research Center on a 9.4 T Magnex (Oxford, UK) magnet (16 cm bore) interfaced to a Bruker (Ettlingen, Germany) BioSpec spectrometer. A 9 cm Resonance Research Inc. (Billerica, MA) gradient insert (500 mT/m in 175 μs) housed dual-purpose imaging gradients and first-order shims, as well as second and third-order shims. An in-house made volume RF coil (ID = 4 cm) was used for signal transmission and reception. To construct a prototype for demonstration of the principles in the passive shim construction, a 50 mL Falcon™ (Becton, Dickinson and Company, Franklin Lakes, NJ) centrifuge tube (OD = 3 cm) was modified to serve as both a mouse bed and base for a shim former. While this setup is not necessarily optimal, as will be described below, it was chosen for both convenience as a natural mouse cradle and its cylindrically symmetric base as the shim former. The coil-cradle assembly was modified to allow for reproducible placement within the magnet bore. The final placement error for this implementation was less than 0.25 mm.

Bismuth (raw pieces) and zirconium (foil, 0.25 mm) metals were acquired from Sigma–Aldrich (Milwaukee, WI). Bismuth elements of $3.2 \times 4.6 \times 1$ mm were formed through melting of the raw pieces (MP = 271 °C) and use of a ceramic mold. Zirconium elements of $3.2 \times 4.6 \times 0.25$ mm were cut from the purchased foil. The optimization grid was constrained to the outer surface of the centrifuge tube. Fig. 2 provides an illustration of the ring placements along the axis of the centrifuge tube. Six rings, each with 16 circumferential element positions were designated. Elements were fixed in position by a custom-machined acrylic former restricting all but the outward radial degree of freedom. A cross-sectional view of the shim former is also presented in Fig. 2. The design included spatial gaps between elements to prevent eddy-current generation over the element ensemble and to allow RF penetration through the assembly.

Magnetic field maps were measured using a conventional gradient-echo mapping technique whereby multiple images were acquired with increasing free-precession delays prior to signal acquisition. [10] Complex phases were calculated relative to the first delay, and by using an extremely short initial delay of 0.25 ms, it could be assumed that the phase difference between the first and second delay was unwrapped. Remaining phases were then temporally unwrapped by extrapolating upon the linear trend established from the first two temporal points. ΔB_0 was then given by a linear least-squares fit of the unwrapped phase versus delay trend.

A stack of two bismuth elements was used as the unit response. Unit responses were measured on a water bottle phantom over 56 adjacent 0.5 mm slices distributed across the water phantom with 56×56 in plane pixels over a 2.8×2.8 cm in-plane field-of-view, five echo delays of 0.0, 0.25, 1.0, 4.0, and 6.0 ms, zero-delay TE = 4 ms, inter-slice TR = 15 ms, and 10 signal averages. Responses were measured for one position on each ring and then computationally rotated to give the other 15 responses for the given ring. This is not a generally applicable method, but was possible for this specific approach because all shim elements for a given ring maintain a constant angle with respect to B_0.

Field map acquisitions were used to empirically validate the approximations presented in Section 2. Approximation 1 was validated by acquiring field maps with (a) a single 2-element bismuth stack in position 1 (see Fig. 2) on the shim former, (b) another single 2-element bismuth stack in position 2 in the same ring on the shim former, and (c) both 2-element bismuth stacks in their respective positions at the same time. The response from acquisitions (a) and (b) were then added together and compared to the response from acquisition (c). Fig. 1A illustrates this experiment and its results.

Approximation 2 was verified by measuring responses from adjacent 3-element bismuth stacks in both (a) a water phantom and (b) *in vivo* in the mouse brain. Fig. 1B summarizes the structure and results of this experiment.

Successful calibration of response ratios through element stacking validated approximation 3. Response scaling according to the solutions for η^* was accomplished by (a) stacking bismuth elements ($\eta_i^* < 0$), (b) stacking zirconium elements ($\eta_i^* > 0$), and (c) stacking zirconium and bismuth

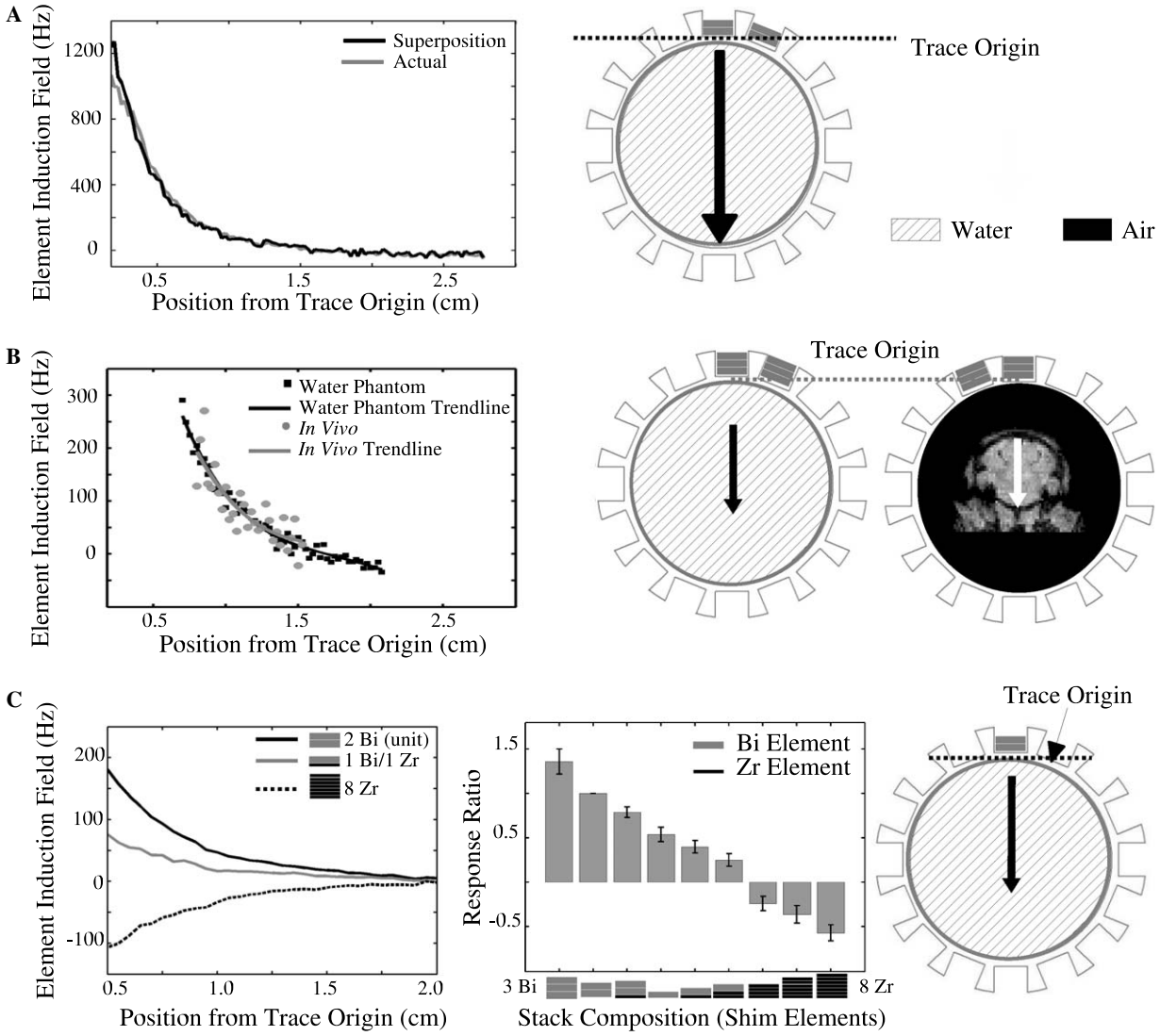

Fig. 1. Validation of approximations utilized in passive shim construction. All traces (left) are indicated in illustrations (right) and begin at the indicated trace origin. (A) Validation of the superposition principle as applied to individual shim element stacks. Magnetic field map traces through a water phantom are shown for both a superposition of individually acquired responses for stacks at the indicated positions (black line), and a response acquired with both stacks in place (gray line). The agreement of the two traces is clear. Notice that a breakdown does become apparent in the immediate vicinity (less than 0.25 cm) of the stack locations. However, a mouse brain will typically start at positions at least 0.7– 0.9 cm radially inward from the shim elements. (B) Validation of shim element induction field independent of sample composition and geometry. Field map traces are shown for the indicated shim element configuration in both a water bottle phantom (black) and the mouse brain *in vivo* (gray). Trendlines are provided to clarify the agreement between the two acquisitions. The increased noise in the *in vivo* acquisition is due to the shorter T_2, reduced water concentration, and a lower filling factor. (C) Results of the calibration procedure. Field map traces through the utilized ROI are shown for 3 element Bi stacks placed in the indicated position 1 on the shim former. Inspection of the traces shows that a constant ratio of the response (measured from zero) induced by 8 Zr and 1 Bi stack configurations relative to the 2 Bi unit response stack is generally maintained. The final calibration results are displayed in the accompanying bar chart. Error bars are given by the standard deviation of the calculated response ratio over the calibration ROI.

elements ($0 < \eta_i^* < 1$). A basis set of possible stack compositions was selected based on spatial limitations (radial direction) of the shim former. In the current construction, this set consisted of nine independent stack compositions. A single position on the shim former was chosen for calibration, and for each stack composition, responses were measured using the aforementioned field mapping procedure. A ROI was selected to closely resemble the *in vivo* brain position, while simultaneously maintaining resolution of individual responses from different stack compositions. For each stack composition, the ratio of its response relative to the unit response was calculated for each pixel within the ROI. The mean of this ratio over the ROI was then used as an effective 'response coefficient' for the given stack composition (corresponding to a value of η^* in the linear composition calculation). Fig. 1C illustrates the calibration procedure. The precision of this calibration procedure is limited by the thickness of individual shim elements composing the stacks (thus determining the number of values for η^* available in the shim construction)

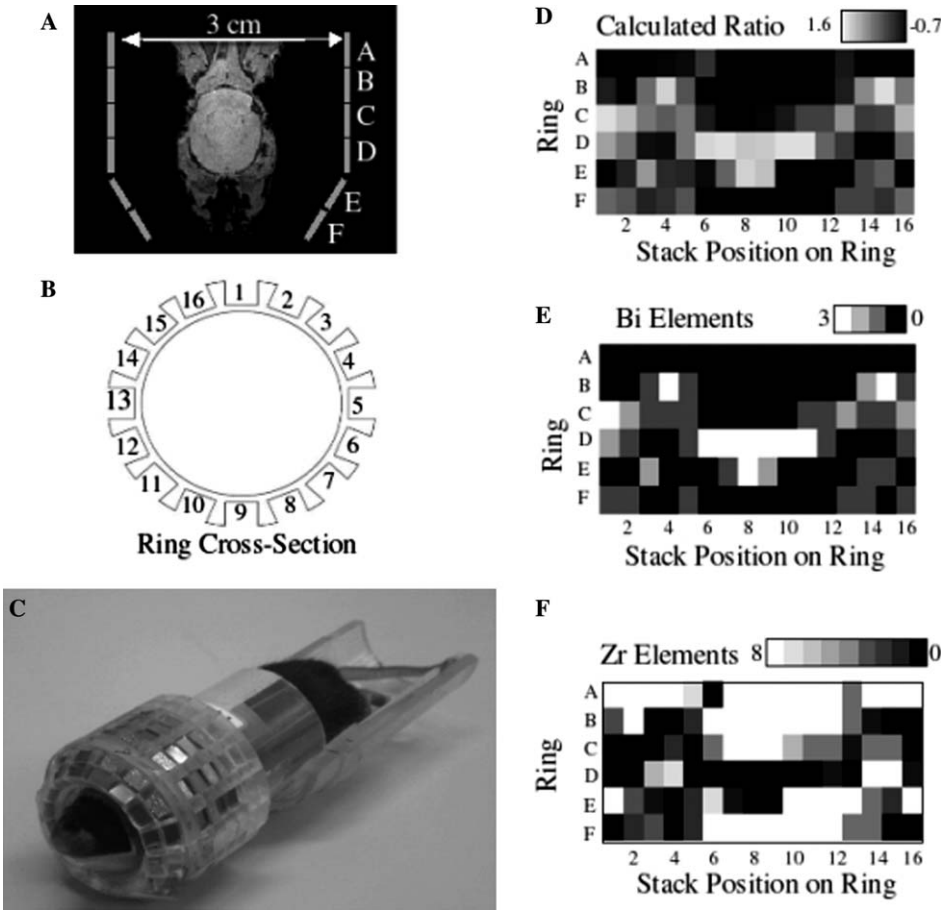

Fig. 2. (A) Illustration of a horizontal cross-section of the mouse-shim system showing the ring positions (labeled by letter) of the constructed shim. (B) A cross-sectional view showing the ring geometry also identifies (labeled by number) positions around the ring where stacks were built. (C) A photograph of the final constructed assembly shows the mouse bed and shim former as constructed. Grayscale images of (D) the calculated stack ratios, (E) corresponding Bi composition, and (F) corresponding Zr composition are presented for visualization of the shim construction. The x-axis in these images represents positions (as labeled in the cross-sectional view) around the ring perimeter and the y-axis specifies rings as indicated in the schematic diagram. From these images, it can be verified that there are consistent patterns and continuity of the calculated stack compositions.

as well as the precision of the field mapping measurements. As will be discussed further, this calibration precision crucially impacts the precision and accuracy of the final shim construction.

In vivo target field maps on the mouse brain (C57 BL, 1 mg/g urethane anesthesia) were acquired in the absence of room-temperature shims over 56 adjacent 0.5 mm slices with a 112×112 data-matrix over 2.8×2.8 cm in-plane field-of-view, TE = 4 ms, interslice TR = 15 ms, and $N = 4$ signal averages. All experiments were conducted in accordance with the Yale Animal Care and Use Committee.

Solutions to Eq. (3) were calculated using constrained least-squares linear optimization software provided by the Matlab (Mathworks, Natick, MA) optimization toolbox. For the previously outlined target-field dimensions, the computation time for optimal coefficient determination was less than 10 s on a standard workstation. Within the current precision of the shim construction, it was found that Zr stacks of more than eight elements had little or no utility in the performance of the shim. Spatial limitations capped the Bi stacks at three elements. Therefore, the optimization software used coefficient constraints of -0.57 (eight element Zr stack) and 1.37 (three element Bi stack). Both of these limiting stack configurations were well below the breakdown point of the utilized approximations. Calculated response coefficients (η^*) were rounded to the nearest available stack configuration determined through the aforementioned calibration procedure. The final shim was then constructed in accordance with these stack compositions.

In vivo diagnostic field maps were measured on $N = 4$ mice (range 21–25 g) with identical acquisition parameters as the target field measurement. Field maps were measured with and without the passive shim in place.

To demonstrate the capability of the system to further homogenize the mouse brain, an alternative shim geometry was proposed with the element former reduced in radius by 2.5 mm. This brought the responses closer to the mouse and allowed the calculation routine to work with steeper induction gradients from each element position. The use of steeper gradients further enables the system to remove

higher-order effects. Note that even in this reduced diameter assembly, the passive shim stacks are still sufficiently removed from the mouse brain to keep approximation 1 valid (see also Fig. 1A and B).

The responses used in this proposed shim demonstration were built from the measured responses through a simple translation in the radial direction. Due to the reduced radius, the number of element positions per ring was also reduced to 12. The resulting compensating field was then computationally built and subtracted from the target field to reveal a field map of the residual homogeneity using the proposed shim. Furthermore, the residual shimmed field using this proposed geometry was also demonstrated using only one metal in the passive shim construction and third-order whole-brain optimized spherical harmonic shims. The feasibility of this proposed shim and the alterations in the calculation procedure needed to reach this level of homogeneity are addressed in Section 5.

Using the diagnostic field maps, global homogeneity was quantified with frequency-offset histograms over the whole brain calculated using 1 Hz bin widths. These distributions did not fit to any simple statistical models. Therefore, distribution widths were determined using the central range containing 80% of the total pixels. This is a generalization of an interquartile range calculation, which uses a 50% criterion [13].

4. Results

Fig. 3 provides field mapping diagnostics of the passive shim system in four slices positioned throughout the mouse brain. Inhomogeneity is significantly reduced in moving from the unshimmed to the passively shimmed map for all slices. The second-order RTS represents the best shimming alternative using previously existing technology on our system. Noticeable improvement is visually recognizable when comparing the passively shimmed field map to the RTS field map. The required coefficients for the added inclusion of third-order shims were roughly 10 times the available shim strengths. This agrees with another recently published third-order shimming analysis on the mouse brain at 9.4 T [14].

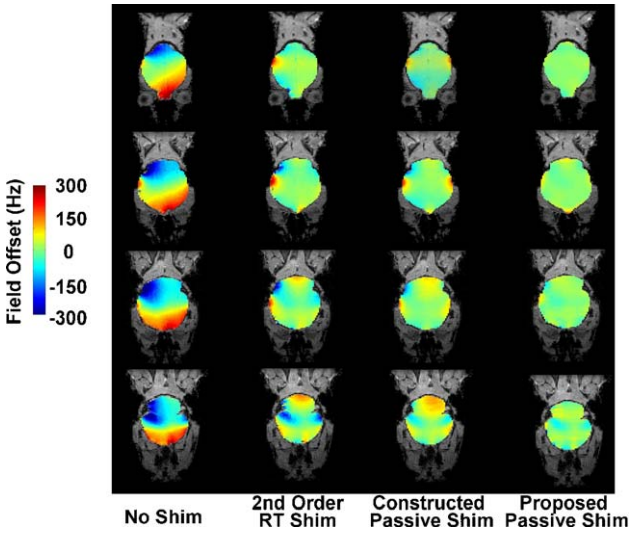

Fig. 3. Field map images demonstrating the utility of the passive shim system over four slices in the mouse brain, spanning a range of 3 mm. RGB colored field maps of brain are embedded in grayscale intensity maps of the mouse head. Homogeneity improvement is gained over existing second-order RTS technology using the constructed passive shim assembly and further improvements are demonstrated with simulations of the proposed shim construction. The simulation shows that residual higher-order effects near the auditory cavities can be damped given increased calibration accuracy and a more advantageous shim grid.

The passively shimmed map possesses residual higher-order homogeneity in close proximity to the auditory and sinus cavities. By moving the shim former closer to the mouse, the computational results of the proposed passive shim construction demonstrate that these effects can be significantly reduced. Fig. 4 provides whole-brain histograms quantifying the utility of the room-temperature shims, the constructed passive shim, and the proposed passive shim. The unshimmed distribution has a width of 320 Hz, which is reduced to 110 Hz using either the second-order RTS or the constructed passive shim, and is further reduced to 40 Hz with the proposed alteration to the passive shim. The roughly similar behavior of the second-order RTS and the constructed passive shim are expected given the low-order limitations within the current construction. While the performance of RT shims cannot be significantly improved due to the restrictions associated with *in vivo* spherical harmonic based shimming, the proposed passive shim demonstrates a clear capacity for further homogenization.

Fig. 5 provides field maps for a single slice within the mouse brain and global histograms for (A) the constructed passive shim and (B) the calculated passive shim used as a basis for the construction. The two field maps show general agreement and the global histograms over the two distributions are quite similar. Along with the results presented in Fig. 1, the overall correspondence between the measured and computed residual field maps supports the methods utilized in the design and construction of the passive shim system. The visually recognizable higher-order discrepancies between the two maps (concealed in the tails of the histograms) are the result of response measurement and calibration imprecision, small variations in animal placement, and manufacturing error. While it is difficult to decouple these sources of error, further discussion in the next section will present solutions to reduce all of them.

The advantages of the two-material passive shimming over both one metal passive shimming and spherical harmonic optimization are presented in Fig. 6. These advantages are best illustrated using the proposed shim system, which can more adequately remove higher-order inhomogeneity. Computational residual field maps from a slice near the auditory cavities are shown for both one and two metal implementations of the proposed shim. A field map from a computational third-order room-temperature shim optimized over the entire brain is also presented.

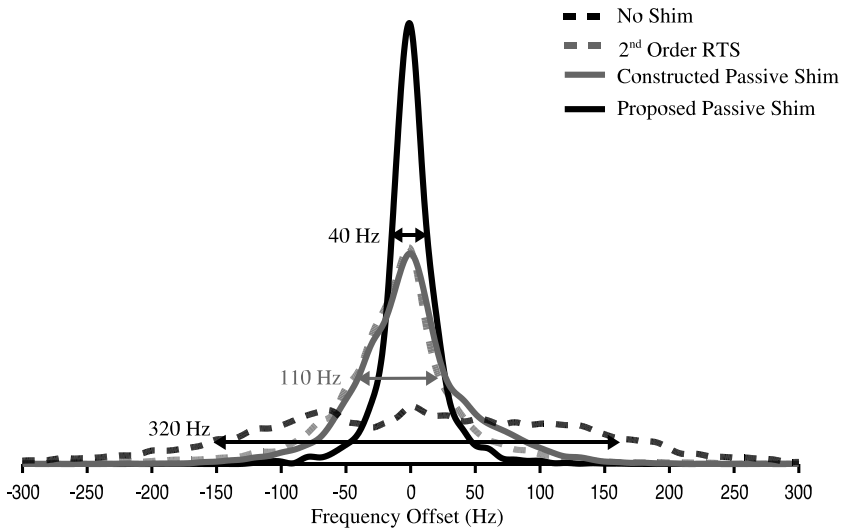

Fig. 4. Whole-brain frequency-offset histograms of diagnostic field map images using the passive shim system. 80% widths of the histograms are displayed.

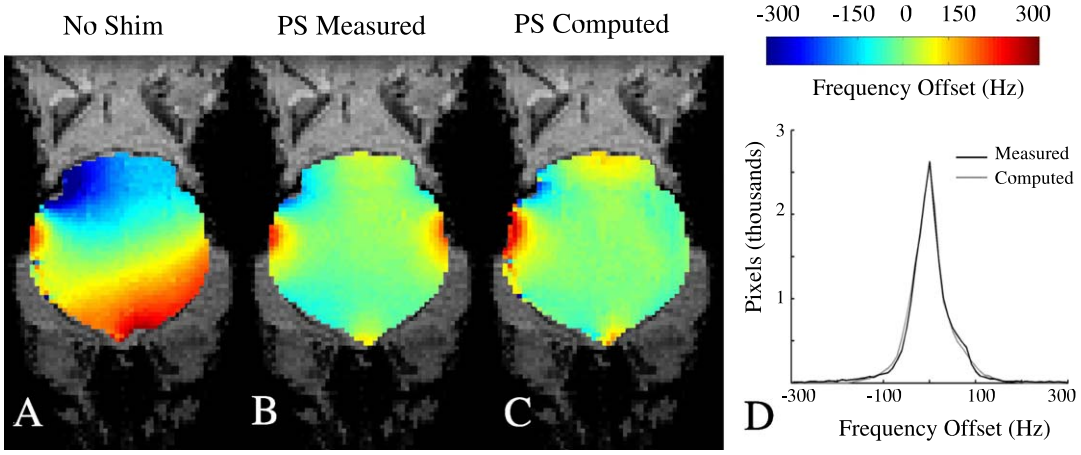

Fig. 5. Field map of a slice in mouse brain (A) with no shimming, (B) measured using the constructed passive shim, and (C) calculated from the response coefficients used in the constructed passive shim. Global histograms over 12 slices are shown in (D). Both histograms have distribution widths of 110 Hz and differ only slightly due to higher-order effects localized to the tails of the distributions. The higher-order differences between the two fields are more readily visible in the field map images. These differences are also typical of the variation found between animals when using the passive shim. Such discrepancies are due to response measurement and calibration imprecision, small variations in animal placement, and manufacturing error. These compromising factors ultimately determine the accuracy and capability of the shim system.

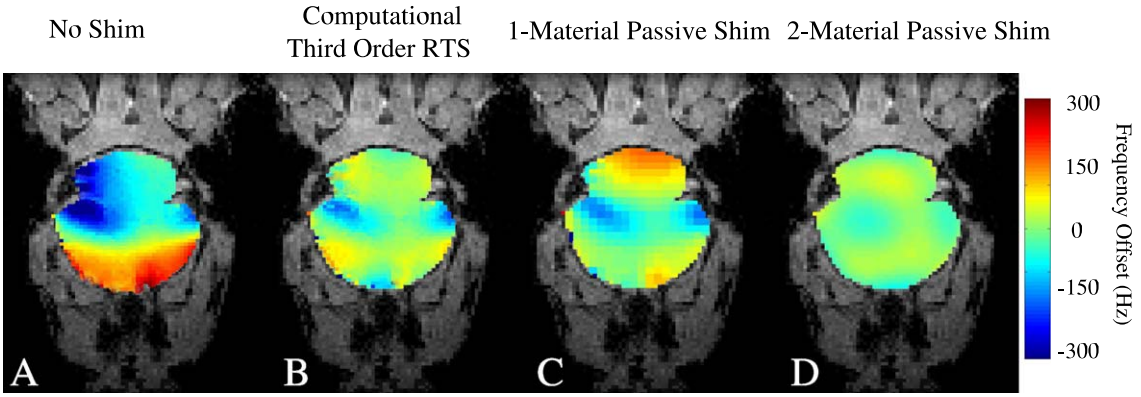

Fig. 6. Reduction of higher-order inhomogeneity by active and passive shimming. Residual magnetic field maps near auditory air cavities are presented using (A) no shim, (B) a computational third-order RTS, (C) a one-material (zirconium) passive shim using the proposed shim geometry, and (D) a two-material passive shim using the proposed shim geometry.

The improved higher-order shimming capacity of the two metal optimization over both the one-metal (Zr) and ideal third-order RTS (using shim strengths well outside the specifications of our state-of-the-art shim system) is visually recognizable, particularly near the sinus and auditory cavities. The one-metal computation was also carried out with Bi, which gave even poorer results. The proposed two-material passive shim clearly outperforms any existing shim platforms for *in vivo* magnetic field homogenization.

5. Discussion

We have presented a novel passive shimming system utilizing two materials of opposing magnetic susceptibility. The theory and methods for the construction of shims using this system have been validated and detailed. Magnetic field map acquisitions have both validated the construction process and diagnosed the utility of the shim. The currently constructed shim has been shown to at least match existing shim technology, and within the framework of the shim construction, the two-metal approach has computationally demonstrated great potential for higher-order spatial field crafting. The shim system is robust and flexible in choices of shim materials and target fields. It further benefits from the geometric freedom gained in using shim elements that do not experience significant torques at high magnetic fields.

Three assumptions in the behavior of induction fields generated by the shim elements make this optimization possible. First, the induction fields from individual elements can be added in linear superposition within the target ROI. Second, it can be assumed that shim element induction fields are primarily a function of the element's susceptibility. Perturbations to this induction field by other susceptible materials in the sample can be neglected. Finally, the ratio of element induction fields to unit responses can be calibrated through stacking of multiple elements. These assumptions are valid over limited stack heights where the stacked inductions do not have significant geometric variation from unit element induction fields.

Field mapping diagnostics have proven the principle and utility of the current shim optimization procedure. Computational analysis has demonstrated the higher-order homogenizing capability of the shim system through a slight alteration in the shim geometry. However, construction of a shim which can robustly remove such higher-order effects requires a number of adjustments to the current shim construction procedure.

First, the spatial noise in the response determinations must be significantly reduced. In the current construction, a compromise was reached between acquisition time and the precision of field maps utilized for shim element response characterizations. The precision of image based field maps benefits from both increased averages and the increased time points used to determine rates of excess phase evolution. However, both of these factors dramatically increase acquisition time. As a result, only one map was measured and then computationally rotated for each of the rings in the current shim construction. Further complicating this issue is the propagation of noise in the stack composition calculation. The optimization function in this calculation is a superposition of scaled responses, which in the current construction resulted in a superposition of 96 field maps. The final result of this superposition possessed precision given by quadrature addition of the precisions of the 96 component field maps. This resulted in significant blurring of the calculation procedure, and a corresponding limitation in higher-order compensation. To sidestep this problem, we are currently investigating computational mechanisms for the determination of response fields. Compared to field map measurements, an approximated computational solution to the magnetostatic boundary problem can have significantly improved spatial resolution, improved precision, and be accomplished within a shorter time-frame. Future work will present detailed methods and results of this computational response determination procedure.

Second, with a large number of positions in the stack placement grid, slight deviations in stack calibration can result in significant variations in the performance of the shim system. The precision of the stack calibration is ultimately limited by (a) the aforementioned response determination precision and (b) the thickness of elements used to effectively 'tune' the stack composition. In the current construction, 0.25 mm thick Zr elements were used for this purpose. To combat higher-order inhomogeneity, computational response determinations will be used in conjunction with significantly thinner Zr foil (0.1 or 0.025 mm, also available from Sigma–Aldrich) to provide significantly improved resolution in the calculation and construction of the stack compositions.

Third, the accuracy of the shim system hinges upon reliable and repeatable placement of the animal with respect to the shim assembly. The current implementation was not constructed to compensate the highest orders of spatial inhomogeneity, and therefore mouse placement was accomplished using the front of the centrifuge tube as a bite bar and then visually aligning the animal. This gave repeatable mouse placement of approximately 1 mm, which in our multiple mouse investigations proved sufficient. Histogram widths calculated over shimmed brains for four measured mice of varying weights (range 21–25 g) gave a mean of 130 Hz with a standard deviation of 23 Hz. However, as the simulations show, future implementations can and will address higher-order effects, and the sensitivity to animal placement will become more stringent. This will require either more flexibility in the shim system or extremely rigid animal placement. Flexibility can be introduced by utilizing basis sets of shims for different animal placements, or allowing for real-time shim construction based on field map acquisitions. Increased placement accuracy and precision will also be investigated using rigid, three-dimensional plastic molds of the mouse head.

Finally, the geometry of the optimization grid is also critical in the precision and capabilities of the shim system. Improvements on the current construction can be made by (a) placing the optimization grid closer to the animal, (b) exploring the use of optimization grids with multiple element sizes and multiple radial positions, and (c) investigating non-cylindrical element placement (i.e., ear bars). None of these approaches will alter the fundamental nature of the optimization procedure.

Passive shims for the mouse brain can mitigate many of the significant problems currently generated by static field inhomogeneity. Specifically, whole-brain echo-planar-imaging (EPI) over the mouse brain currently requires the use of spin echo or multiple-interleave gradient echo acquisition strategies. Such restrictions limit the time resolution of whole-brain fMRI and DTI studies [15]. Higher-order passive shimming can significantly reduce these limitations and enable viable single shot gradient-echo EPI over the entire mouse brain. Within the transgenic mice phenotyping community, passive shims could be particularly beneficial when used in conjunction with recently developed multi-animal acquisition protocols [12]. In these multi-animal systems, spherical harmonic shims cannot be used, since they will strongly degrade the homogeneity over most mice while attempting to improve the homogeneity of one animal. The current optimization procedure could be readily expanded to develop passive shim arrays that can be used in conjunction with RF coil arrays to improve the performance of multiple-animal MR studies.

Since intra-subject inhomogeneity varies significantly within the human brain, extension of the passive shim system to human studies will require more flexibility in element configuration. Detailed investigations into the required degree of such flexibility are in progress. Rapid utilization of the shim could be implemented with a basis set of shims optimized to fit certain sizes and shapes of subjects. Furthermore, since the computational optimization of element locations and stack configurations for specific target fields requires only seconds on a standard workstation computer, the shim could be individualized on a per-subject basis. Such individualized shims could be optimized in a matter of minutes through field map acquisitions and manual alteration of a reasonable-sized shim grid. The extension of the presented shim construction to humans could also require stronger magnetic materials.

A final consideration in the use of metallic passive shims concerns RF penetration and heating. By using discrete arrays of shim elements instead of continuous sheets of metal, we have alleviated this concern. B_1 mapping experiments have validated this approach by showing no significant RF variation with and without the use of the current shim construction. Temperature measurements were also taken directly from the shim elements to address RF heating concerns. No measurable temperature change was recorded after running a standard gradient-echo imaging sequence for 45 min with the shim system in place.

This work has demonstrated the viability of an alternative approach to *in vivo* static field homogenization. Experimental results have verified the accuracy of the construction procedure and computational projections have shown that the system is not limited to low-order compensation. Further work will include the construction of a shim for higher-order compensation in the mouse brain, development of shims for surface coil assemblies, and extension of the shimming system to human studies.

Acknowledgments

This work is funded by NIH Grants R21 CA118503 and R01 EB002097. The authors would also like to thank Amy Scouten for editing assistance.

References

[1] K.M. Koch, S. McIntyre, T.W. Nixon, D.L. Rothman, R.A. de Graaf, Dynamic shim updating on the human brain, J. Magn. Reson. 180 (2006) 286–296.
[2] R.A. de Graaf, P.B. Brown, S. McIntyre, D.L. Rothman, T.W. Nixon, Dynamic shim updating (DSU) for multislice signal acquisition, Magn. Reson. Med. 49 (2003) 409–416.
[3] A.M. Blamire, D.L. Rothman, T.W. Nixon, Dynamic shim updating: a new approach towards optimized whole brain shimming, Magn. Reson. Med. 36 (1996) 159–165.
[4] G. Morrell, D. Spielman, Dynamic shim updating (DSU) for multislice magnetic resonance imaging, Magn. Reson. Med. 38 (1997) 477–483.
[5] J.J. Hsu, G.H. Glover, Mitigation of susceptibility-induced signal loss in neuroimaging using localized shim coils, Magn. Reson. Med. 53 (2005) 243–248.
[6] C.N. Chen, D.I. Hoult, Biomedical magnetic resonance technology, Adam Hilger, New York, 2005.
[7] J.L. Wilson, M. Jenkinson, P. Jezzard, Optimization of static field homogeneity in human brain using diamagnetic passive shims, Magn. Reson. Med. 48 (2002) 906–914.
[8] A. Jesmanowicz, J.S. Hyde, W.F.B. Punchard, P.M. Starewicz, Method for shimming a magnetic field in a local MRI coil, US Patent 6,294,972 (2001).
[9] J.F. Schenck, The role of magnetic susceptibility in magnetic resonance imaging: MRI magnetic compatibility of the first and second kinds, Med. Phys. 23 (1996) 815–850.
[10] E.M. Haacke, R.W. Brown, M.R. Thompson, R. Venkatesan, Magnetic Resonance Imaging: Physical Principles and Sequence Design, John Wiley and Sons, New York, 1999.
[11] CRC Handbook of Chemistry and Physics, CRC Press (2004).
[12] J. Dazai, N.A. Bock, B.J. Nieman, L.M. Davidson, R.M. Henkelman, X.J. Chen, Multiple mouse biological loading and monitoring system for MRI, Magn. Reson. Med. 52 (2004) 709–715.
[13] D.J. Sheskin, Handbook of Parametric and Nonparametric Statistical Procedures, CRC Press, Boca Raton, FL, 2000.
[14] N. Miyasaka, K. Takahashi, H.P. Hetherington, Fully automated shim mapping method for spectroscopic imaging of the mouse brain at 9.4 T, Magn. Reson. Med. 55 (2006) 198–202.
[15] J.L. Andersson, M. Richter, W. Richter, S. Skare, R.G. Nunes, M.D. Robson, T.E. Behrens, Effects of susceptibility distortions on tractography, Proc. ISMRM 11 (2004) 87.
[16] J.P. Marques, R. Bowtell, Application of a Fourier-based method for rapid calculation of field inhomogeneity due to spatial variation of magnetic susceptibility, Concepts in Magn. Res. B. 25 (2005) 65–78.
[17] R. Salomir, B.D. de Senneville, C.T.W. Moonen, A fast calculation method for magnetic field inhomogeneity due to an arbitrary distribution of bulk susceptibility, Concepts in Magn. Res. B 19 (2003) 26–34.